10-18-2023

Biomimetic nacre-like aramid nanofiber-holey MXene composites for lithium-sulfur batteries

Yuying Wang

Volkan Cecen
Rowan University

Shoupeng Wang

Lei Zhao

Li Liu

See next page for additional authors

Cell Reports
Physical Science

CellPress
OPEN ACCESS

Article

Biomimetic nacre-like aramid nanofiber-holey MXene composites for lithium-sulfur batteries

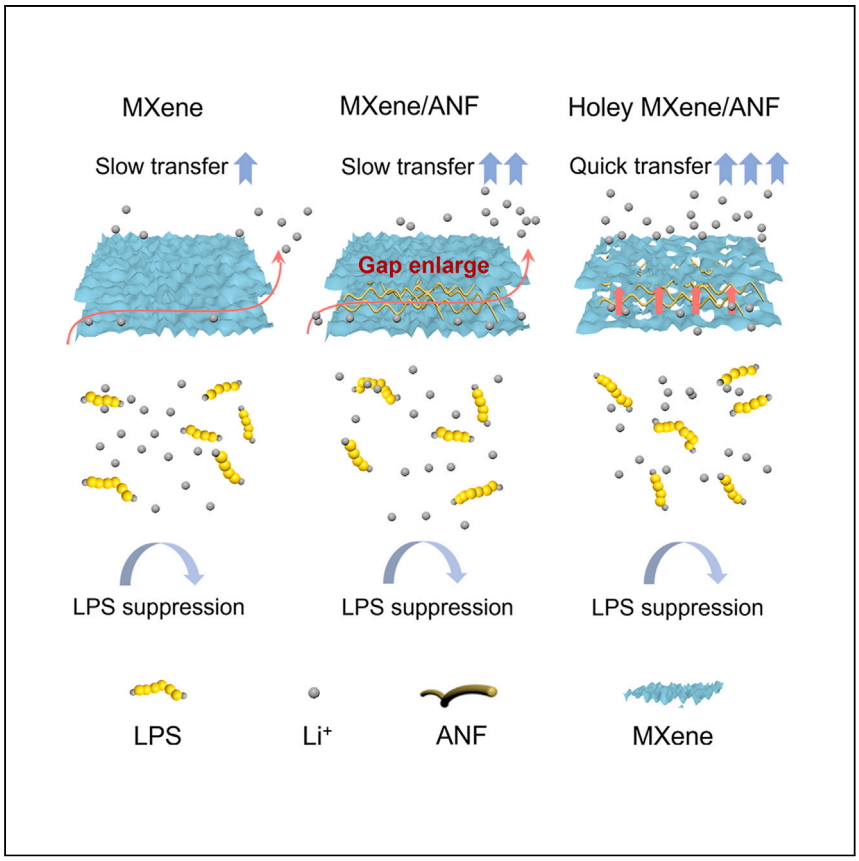

Wang et al. report a biomimetic multifunctional composite separator with a multilayer film consisting of porous $Ti_3C_2T_x$ (MXene) nanosheets bonded with aramid nanofibers. It shows efficient lithium-ion transport and remarkable stability in long-term cycling when applied in lithium-sulfur batteries.

Yuying Wang, Volkan Cecen, Shoupeng Wang, ..., Xiaonan Zhu, Yudong Huang, Mingqiang Wang

huangyd@hit.edu.cn (Y.H.)
mqwang@hit.edu.cn (M.W.)

Highlights

A "brick-and-mortar" multifunctional biomimetic composite is proposed

Holey $Ti_3C_2T_x$ shortens the ion transport distance compared with $Ti_3C_2T_x$

The functional groups of holey $Ti_3C_2T_x$ and ANF inhibit the shuttle effect of LPS

Wang et al., Cell Reports Physical Science 4, 101592
October 18, 2023
https://doi.org/10.1016/j.xcrp.2023.101592

Cell Reports
Physical Science

CellPress
OPEN ACCESS

Article

Biomimetic nacre-like aramid nanofiber-holey MXene composites for lithium-sulfur batteries

Yuying Wang,[1,5] Volkan Cecen,[2,5] Shoupeng Wang,[1] Lei Zhao,[1] Li Liu,[1] Xiaonan Zhu,[3] Yudong Huang,[1,*] and Mingqiang Wang[1,4,6,*]

SUMMARY

Polysulfide shuttle and lithium dendrite formation limit practical applications of lithium-sulfur (Li-S) batteries. To address these issues, we propose a nacre-inspired design of MXene/aramid nanofiber (ANF) separator with "brick-and-mortar" microstructure. The combination of shortened ion transfer distance generated by holes on MXene and enlarged interlayer spacing provided by ANFs creates a hierarchical ion path "highway" that modulates the efficiency of ion transportation while synergistically suppressing the polysulfide shuttles. Furthermore, benefitting from the introduction of ANF, the composite membrane has good mechanical properties and impact tolerance. With simultaneous mitigation of dendrite growth and polysulfide poisoning of anodes, the cells with nacre-inspired separator exhibited excellent rate capability to 5 C and had a possible long cycle life of 3,500+ cycles with capacity decay of 0.013% per cycle to 3 C. This work offers a membrane design strategy inspired by the structure of pearl layers, aiming to resolve materials performance challenges of high-performance energy storage.

INTRODUCTION

Lithium-sulfur (Li-S) batteries have gathered an enormous amount of attention due to their high theoretical specific capacity (1,675 mA h g^{-1}) at low cost, combined with the earth abundance of elements and environmental friendliness.[1–3] Despite these exhilarating advantages, their implementation has been hampered by some knotty issues relating to soluble lithium polysulfide (LPS) crossover, low sulfur loading, and uncontrolled lithium dendrite growth upon cycling, resulting in unsatisfactory cycle life and inferior Coulombic efficiency (CE).[4–6] In the past, many attempts have been dedicated to alleviating those issues, and one of the widely applied directions was given to designing the structure of sulfur cathode. It was shown that encapsulating sulfur into carriers made from microporous nanocarbons,[7] graphene,[8] CNTs,[9] metal-organic frameworks,[10] or transition metal oxides[11] can effectively minimize LPS release. However, the limited physical adsorption capacity and binding interaction sites especially under the high sulfur loading still make it hard to achieve high performance with satisfactory energy density.[2,12,13] Another efficient strategy is constructing a protective layer on the surface of the Li anode, which can validly block the side reaction between Li and LPS.[14] However, the extra solid-electrolyte layer between the anode and electrolyte will undoubtedly increase the interfacial resistance, leading to a poor rate capability. Therefore, it seems that multifunctional separators are a more feasible way for achieving high-performance Li-S batteries because they not only can serve as an electronic insulator but also can control the transport of ions.[15–17]

[1]School of Chemistry and Chemical Engineering, MIIT Key Laboratory of Critical Materials Technology for New Energy Conversion and Storage, State Key Laboratory of Urban Water Resource and Environment Harbin Institute of Technology, Harbin 150001, P.R. China

[2]Department of Chemical Engineering, Rowan University, Glassboro, NJ 08028, USA

[3]Wuxi HIT New Material Research Institute Co., Ltd, Wuxi 214100, Jiangsu, P.R. China

[4]Key Laboratory of Advanced Materials of Ministry of Education, Beijing 100084, China

[5]These authors contributed equally

[6]Lead contact

*Correspondence: huangyd@hit.edu.cn (Y.H.), mqwang@hit.edu.cn (M.W.)

https://doi.org/10.1016/j.xcrp.2023.101592

Having noticed the potential function of separators, significant efforts and works in this direction have been applied by using coatings such as carbonaceous materials, metal-oxide, and ceramic nanoparticles[18–21] on a polyolefin separator because of their excellent LPS suppression. However, the current dilemma is that the excessively tightly stacked state of coating materials generally hinders the rapid transmission of Li^+ ions inside the separator, especially in the vertical direction since the overall ion path channel is lengthened or blocked, while high ion transport is critical to have the high energy density in Li-S batteries for practical applications. Meanwhile, the coating materials generally cannot offer enough protection for these separators against external impacts due to the characteristics of mechanical brittleness. Besides these constraints, a rational separator should also have low shrinkage and good resistance to heat to prevent short circuit and fire. Therefore, it is still challenging to develop a multifunctional separator that cannot merely suppress LPS crossover and dendrite growth but that also can provide efficient ion transport and support the practical cells for long-term cycling under high sulfur loading.

Looking for a materials design solution for a separator of Li-S batteries, one could notice that the challenges of contrarian materials properties are not unique to these devices. In fact, the struggle to create a material with multiple functional properties is known exceptionally well in the world.[22] An example is the "brick-and-mortar" microstructure in the nacre.[23,24] Unlike the inherent brittleness of disordered nanoparticle assemblies, the sliding and deflection of highly aligned platelets can dissipate external forces, making nacre excellent in toughness and impact resistance despite its high inorganic ceramic content (95%).[25,26] However, realizing a high-performance Li-S battery remine needs the high efficiency of ion transportation, and synergistically it can block the polysulfide shuttles.

Hence, inspired by the natural nacre structure, we report a biomimetic multifunctional composite separator via preparing a multilayered membrane consisting of the holey Ti_3C_2Tx (MXene) nanosheet bonded by aramid nanofiber (ANF) instead of the typical nanoparticle coating. The ultra-strong structural ANF not only serves as an insulating layer to avoid the contact between two electrodes, but it also acts as an intercalating and interlocking agent that can enhance the mechanical strength and expand the interlayer channel to prevent the restacking of adjacent 2D MXene nanosheets. Moreover, benefitting from the significantly shortened ion transport distance provided by the etching holes on the MXene surfaces, the composite membrane also displays a high ionic conductivity of 0.42 ± 0.02 mS cm^{-1} (220% higher than that of MXene, 0.19 ± 0.001 mS cm^{-1}), good mechanical properties with Young's modulus of $E = 5.6 \pm 0.3$GPa (4.0 and 30 times higher than MXene and Celgard 2400, respectively), high thermal stability (600°C), and excellent electrolyte wettability. Meanwhile, the composite membrane is also remarkably effective in depressing the shuttle effect of soluble LPS because of the strong interaction of polysulfide species with MXene functional groups.[27] Such a combination of properties found in the nacre-inspired holey MXene/ANF (HMA) composite resulted in high efficiency in blocking LPS, efficient Li^+ ion transport, and remarkable stability over long-term cycling in a Li-S battery. As a result, the assembled battery possesses a super rate capability up to 5.0 C, low-capacity fading rates of approximately 0.013% per cycle over 3,500 cycles, and high reversible specific/areal capacity of 6.1 mAhcm^{-2} at a high sulfur loading of 6.0 mg cm^{-2} with sparing electrolyte, which demonstrates intriguing potential for practical applications.

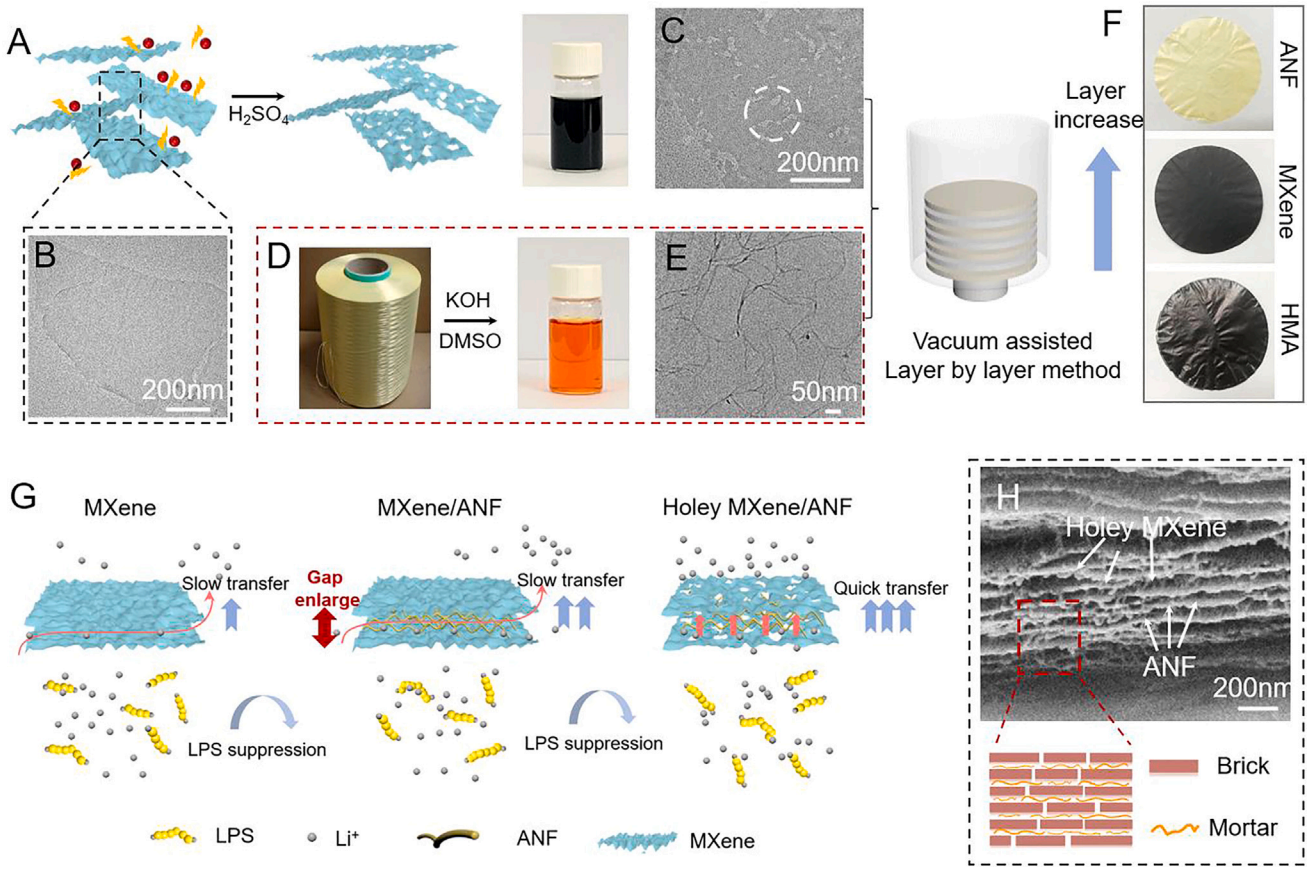

Figure 1. Schematic fabrication process of the HMA membrane

(A) The fabrication process of a holey MXene nanosheet from MXene.

(B and C) TEM images of the as-prepared MXene and holey MXene nanosheets.

(D) The ANF is prepared from commercial Kevlar yarns.

(E) TEM image of the as-prepared ANF.

(F) Photograph of as-obtained ANF, MXene, and HMA membrane.

(G) Schematic of ion transport in different separator.

(H) Cross-section SEM images of HMA membrane.

RESULT AND DISCUSSION

Characterization of the HMA membrane

The extended ion pathway in restacked 2D materials significantly reduces the electrochemical performance of the MXene-based separators. Therefore, it appears that etching holes on the MXene sheets is an efficient method of resolving the ion transport issue by creating shortcuts in the restacked layer. The holes on the MXene sheets of several nanometers in diameter were generated by etching the $Ti_3C_2T_x$ surface with H_2SO_4 solution as reported previously[27] (Figures 1A–1C and S1). The etching process can create the hierarchical nanoporous structure (15–30 nm) (Figure S1) and various functional groups (–OH, –O groups) on the basal plane of MXene (Figure S2A), which contribute to the shortened ion pathway in restacked film and enhanced adsorption energies toward Li_2Sx ($1 \leq x \leq 8$).[28–30] The mortar of ANF 10–20 nm in diameter (Figures 1D and 1E) was prepared in dispersions in dimethyl sulfoxide (DMSO).[31] The functional groups (C−N, C=O, and COOH) on ANFs become available to interact with the hydroxyl groups on MXene, which improves nanofiber-nanosheet stress transfer (Figure S2B). Both holey MXene and ANF can form a stable suspension in DMSO solvent (Figure 1A). We used a novel

vacuum-assisted layer-by-layer assembly process to prepare the nacre-inspired multilayers of HMA membranes (Figure 1F). This method has nanoscale precision of structural engineering of nanocomposites with excellent uniformity, which is essential for elimination of the nanoscale "weak spots" of the membrane.[32]

The experimental studies in this work are focused on the elucidation of trends in mechanical properties and ionic conductivity as they relate to the 2D architecture of the nanocomposites. Evaluation of the mechanics of the laminar composites *in silico* saves time and avoids structural dilemmas when targeting specific properties. An example is the simultaneous attainment of high ionic conductivity and high stiffness[33,34] leading to the opposite structural requirements of materials. The same is true for high mechanical strength and high ion intercalation capacity,[35] an equally important pair of properties for structural batteries. This clash of properties can be cumulatively described as the load-bearing functionality requiring strong chemical bonds and dense robust materials, whereas charge transport and storage functionalities require weak chemical bonds and porous, deformable materials. Thus, we systematically investigated the effect of ANF content on the mechanical stiffness and the ionic conductivity of HMA membranes. Considering the results shown in Figure 2A, typical 20 wt % ANF-containing HMA membranes have a realistic possibility of offering a variety of composites with a combination of high strength and high ionic conductivity. Specifically, ANF (20 wt %) was selected as the insulation layer at both the top and bottom outermost surfaces, while holey MXene (80 wt %) acted as a middle absorption layer. The multilayered architecture of HMA could be prepared by evenly dividing into different numbers of holey MXene and ANF layers, and the typical lamellar microstructure clearly can be observed through the cross-sectional scanning electron microscope (SEM) images and the corresponding energy dispersive X-ray spectroscopy images (Figure S3). Obviously, a gradual increase in the number of layers of the membrane gives rise to improved tensile strength due to the good dispersion. Based on the correlation between the layer's number and tensile strength, the range of layers was chosen to be around 155 and used in the following study (Figure S4). The obtained paper-like, thin membrane was highly flexible, indicating structural integrity (Figure S5). The top view of the SEM image of HMA presents a smooth surface (Figure S6), and the cross-sectional image reveals a well-stacked, ordered lamellar structure (Figures 1H and S7). Similar to the "brick-and-mortar" of nacre, the layered organization of the soft and hard structural blocks offers high mechanical properties to the material. Moreover, the negative charge of ANF enlarges the interlayer spacing between holey MXene nanosheets and prevents its restacking, further benefitting the ion transport (Figure 1G). Notably, the thickness of HMA could be easily changed by adjusting the amount of the dispersion used for filtration and be simultaneously much thinner than that of a Celgard 2400 separator with a thickness of 30 μm (Figures S8 and S9). Reduction of separator thickness is also of importance and needed to avoid high internal resistance inside the battery and to increase the mass energy density. Moreover, the HMA also displays a higher heat resistance (Figure S10) and lower thermal shrinkage (Figure S11) in comparison to the Celgard 2400.

Synergistic effects of holey MXene and ANF of HMA

The weight content of ANF also has a significant influence on the mechanical properties and ionic conductivity of a composite membrane. Apparently, the tensile strength of HMA composite membrane is enhanced by the increasing ANF content[36,37] (Figure 2A). The excellent mechanical properties are ascribed to the extensive hydrogen bonding interactions between the nanofiber and the nanosheet, where the fibrous ANFs are interconnected to the face of the holey MXene and bind

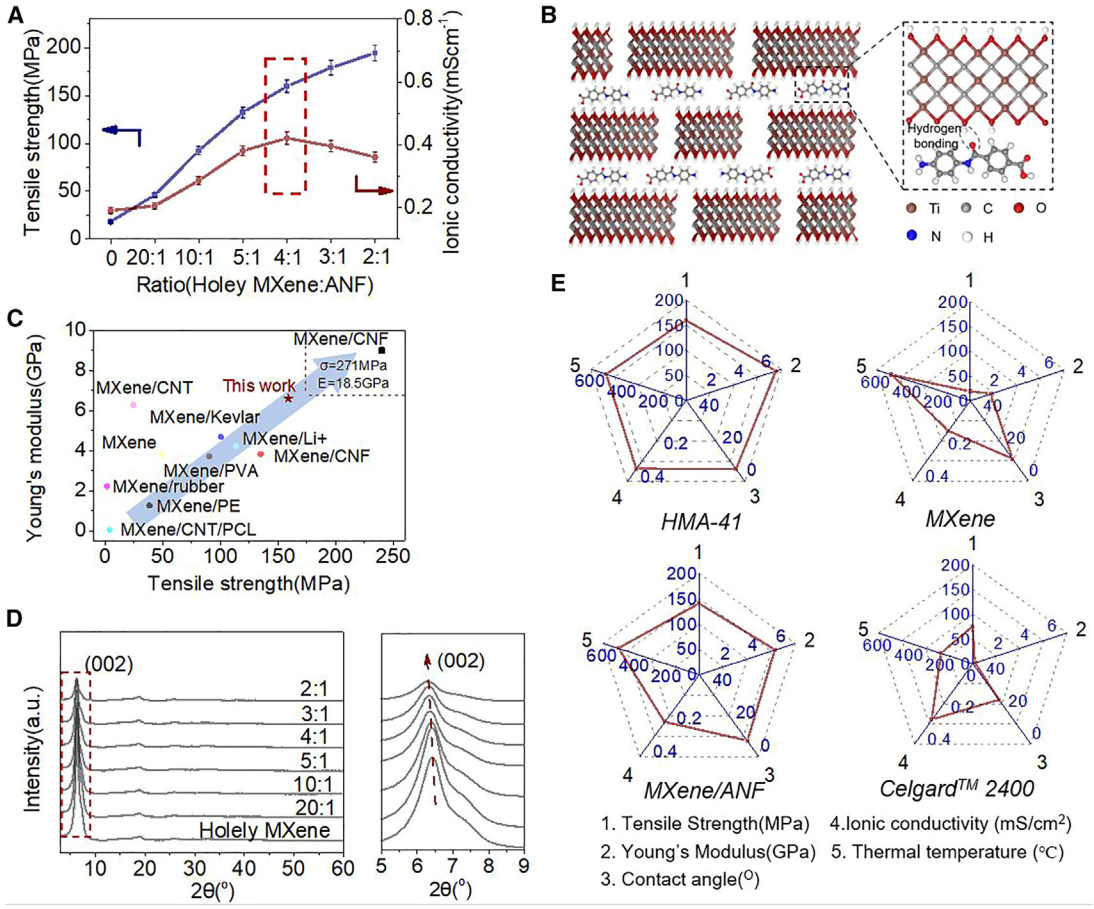

Figure 2. The properties of HMA-41 composite membrane

(A) Characterization of tensile strength and ionic conductivity of HMA membrane with various ANF weights from 20:1 to 2:1. error bar ±5%

(B) Schematic of the interior structure of the HMA composite membrane.

(C) Comparison of strength and modulus of reported MXene-based membrane materials.

(D) XRD patterns of HMA with different ANF contents.

(E) Multiparameter comparison of various membranes based on glyph plots.

the holey MXene nanosheets to each other (Figure 2B).[36,37] Meanwhile, the ion transfer of Li^+ in the composite membrane also first increases and then reaches a maximum value on increasing the ANF ratio to 4:1. This is attributed to the ANF expanding the interlayer space between holey MXene nanosheets, benefitting the ion transport through the nanosheet (Figure 1G). This phenomenon can be further demonstrated by XRD results (Figure 2D) as a result of the peak of (002) shift to lower angle.[36,37] However, continuously increasing the proportion of ANF will partially block the ion transport nanochannel and introduce a physical barrier, leading to a reduction in efficiency of ion transfer (Figure S12). Based on these parameters, the optimal weight ratio of holey MXene:ANF was chosen to be 4:1; this composite was denoted as "HMA-41" and is used throughout this study. The resulting HMA-41 revealed a unique combination of mechanical and ionic conductivity properties. The tensile strength (σ), Young's modulus (*E*), and toughness (Γ) were 159 ± 6.9 MPa, 6.6 ± 0.2 GPa, and 3.8 ± 0.16 MJ m^{-3}, respectively (Figure S13 and Table S1), which is competitive and exceeds that of most reported MXene-based membranes and stacked pristine 2D materials (Figure 2C and Table S2).[38–40] Given the MXene membrane (E = 1.6 ± 0.08 GPa) and Celgard 2400 (E = 0.17 ± 0.01 GPa),

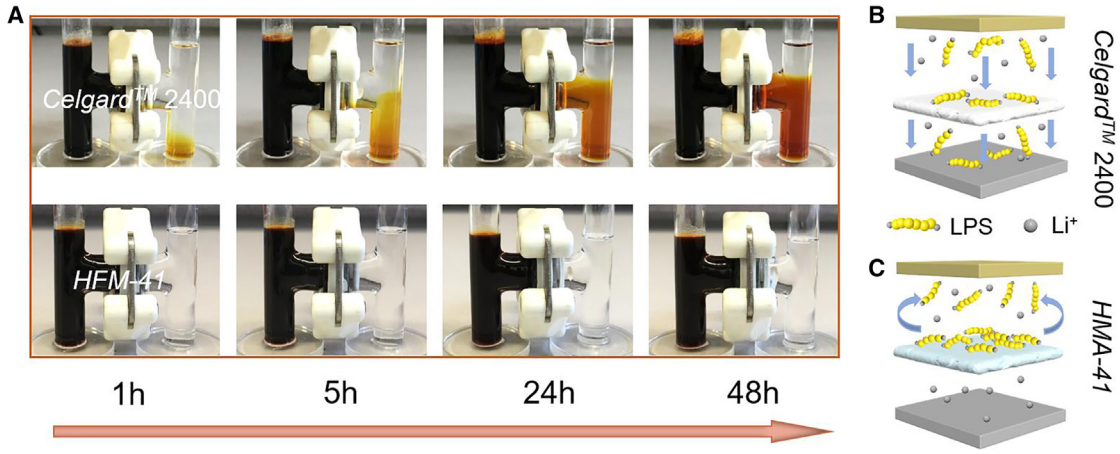

Figure 3. Polysulfide-blocking capability of the HMA-41 separator

(A) Diffusion of LPS in H-type cell through Celgard 2400 and HMA-41 separator.

(B and C) Schematic representation of Celgard 2400 and HMA-41 ion-selective separator that acts as an ionic sieve against LPS.

it shows a 4.0-fold and 35-fold higher Young's modulus. Ionic conductivity of HMA-41 is 0.42 $\pm$ 0.02 mS cm^{-1}, which is 220% higher than that of MXene/Celgard 2400 of 0.19 $\pm$ 0.001 mS cm^{-1} and slightly higher than Celgard 2400 of 0.35 $\pm$ 0.02 mS cm^{-1} (Figure S14), indicating synergistic enhancement of properties of the ion path "highway" from holey MXene itself and the large nanoscale channels with negative charge imparted by ANF (Figure 1G). The good electrolyte wettability, high porosity, and high electrolyte uptake of HMA-41 further decrease internal resistance, which is also needed to obtain superior charge and discharge rate (Figure S15 and Table S3).

The shortest ion transport distances originated from the porous structure on the MXene surface, and the coexistence of space charge brought by the insertion of the ANF interlayer[32,41] is expected to enhance the ion selectivity and promote the ion transport.[41,42] We demonstrated that HMA-41 separators effectively suppressed the transport of LPS from cathode to anode compartments. An H-type glass cell was employed to visualize the role in preventing the diffusion of LPS solution (0.5 M Li_2S_4 in 1,3-dioxolane/dimethoxyethane [v/v = 1/1] solvent). Driven by the concentration gradient, LPS quickly diffused across the Celgard 2400, and the right chamber turned from colorless to dark brown within a few hours (Figure 3A). In contrast, the diffusion of LPS was significantly blocked by the HMA-41 membrane, and the right chamber remained colorless even after 48.0 h (Figures 3B and 3C). This phenomenon can be further demonstrated by the self-discharge study, in which HMA-41 has a stable voltage curve, while a decreasing curve was observed in Celgard 2400 (Figure S16).

Electrochemical characterization

These key performance assessments from separator are necessarily required for high-performance Li-S batteries, which including tensile strength, tensile modulus, thermal stability, ionic conductivity, electrolyte wettability, and Li-ion diffusion coefficients. Since battery performance varies with these metrics, the total area enclosed by the glyph plot can be used as a cumulative capability criterion for reflecting and optimizing the performance of batteries. The evaluation displays the batteries with HMA-41 have across-the-board performance exceeding that of the MXene/ANF, MXene/Celgard 2400, Celgard 2400, and most of the current separators in Li-S

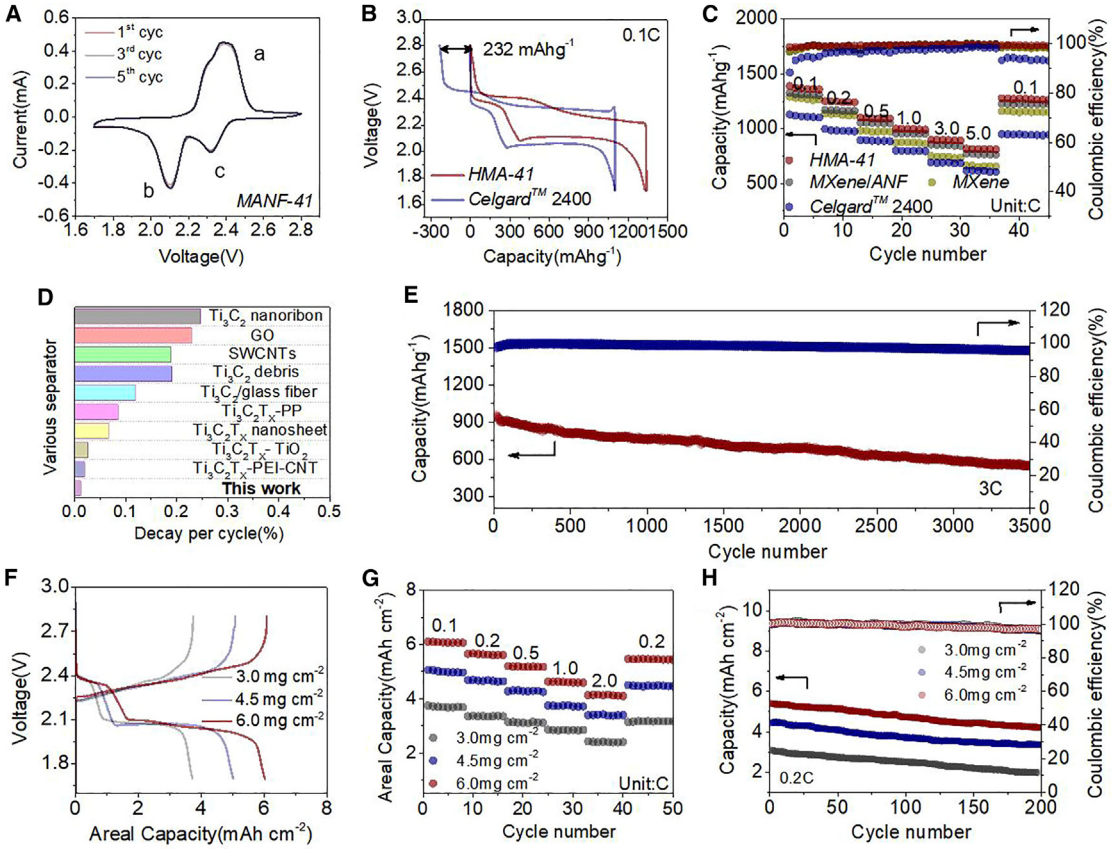

Figure 4. Electrochemical performance of the Li-S batteries

(A) CV profiles with HMA-41 at a scan rate of 0.1 mVs^{-1}.

(B) Galvanostatic charge-discharge profiles of HMA-41 and Celgard 2400 separator at a rate of 0.1 C.

(C) Rate performance of Li-S batteries ranging from 0.1 to 5.0 C with HMA-41, MXene/ANF, MXene/Celgard 2400, and Celgard 2400 separators.

(D) The decay per cycle comparison of Li-S batteries with various MXene-based Li-S batteries.

(E) Cycling performance of Li-S batteries with HMA-41 separator at a rate of 3.0 C after 3,500 cycles at the sulfur loading of 1.2 mg/cm^2.

(F) Galvanostatic charge-discharge profiles of HMA-41 at a rate of 0.1 C at different sulfur loadings.

(G) Rate performance of Li-S batteries with HMA-41 at different sulfur loadings.

(H) Cycling performance comparison of Li-S batteries with HMA-41 separator at different sulfur loadings.

batteries, indicating the HMA-41 is a good candidate as a separator for Li-S batteries (Figure 2E).

Moreover, as the HMA-41 separator impeded the side reactions between anode and LPS, the discharge capacity increased due to the active material loss being reduced. Therefore, the initial discharge capacity of 1,340 mAh g^{-1} was achieved on the cell with HMA-41, much higher than that of cell with Celgard 2400 of 1,084 mAh g^{-1} (Figure 4B). Consistent with the CV curve (Figure 4A), the charge/discharge curve consisted of one oxidation plateau and two reduction plateaus, representing the redox reactions of a Li-S battery.[20] The highly efficient Li^+ transport through HMA-41 can translate into superior rate capability of an Li-S battery (Figures 4C and S17). With the current rates varying from 0.1 to 5.0 C, the capacities of 1,340, 1,248, 1,095, 995, 893, and 818 mAh g^{-1} were observed, much superior to cells with Celgard 2400, MXene/Celgard 2400, and MXene/ANF. Although the voltage plateaus of cells with an HMA-41 separator decrease obviously at the high current rate, the sloping shape was almost unchanged (Figure S17), and a high capacity of around 62.5% was retained, which evidenced the fast ion transport. When the current rate

was recovered to 0.1 C, a high capacity of 1,276 mAh g^{-1} was obtained and almost kept stable in the following 100 cycles, whereas 1,230 mAh g^{-1}, 1,165 mAh g^{-1}, and 958 mAh g^{-1} were detected for the cells with MXene/ANF, MXene/Celgard 2400, and Celgard 2400 separators, and only 1,098 mAh g^{-1}, 1,011 mAh g^{-1}, and 648 mAh g^{-1} can be maintained after 100 cycles, respectively (Figure S18). Penetration of LPS across separators also had detrimental effects for CE, with only 85% being retained for the cell with Celgard 2400 after cycling 100 times at 0.1 C compared to 99% with HMA-41 (Figure S18). Moreover, the capacity decay rate per cycle was also increased from 0.08% for HMA-41 to 0.31% for Celgard 2400, exhibiting a higher cycle stability of HMA-41. Meanwhile, the cycling stability as well as the CE could be further improved by increasing the thickness of HMA-41, while the long diffusion path length and internal resistance will weaken the initial capacity of batteries[43] (Figure S19). The effect of HMA-41 on the battery's electrochemical kinetics before and after cycling is also evaluated by electrochemical impedance spectra (EIS) measurement (Figure S20). The EIS spectra for the batteries with Celgard 2400, MXene/Celgard 2400, or HMA-41 separators before and after cycling are modeled with equivalent circuits. Prior to cycling, the batteries with HMA-41 had a lower resistance compared to Celgard 2400 and MXene/Celgard 2400, which is expected from the shorter ion transfer distance and expanded ion channel in the separator (Figure S21A). Also, the R_{ct} value of the cells with HMA-41 and MXene/Celgard 2400 decreased after 100 cycles (Figure S20B) due to electrolyte infiltration and chemical activation of the active materials.[44] However, cells with Celgard 2400 displayed two semicircles after cycling, where the first semicircle of R_{sf}//CPE_{sf} was associated with the formation of a solid Li_2S_2/Li_2S insulating layer on the lithium anode,[45] while the second semicircle of R_{ct}//CPE_{ct} was derived from the charge transfer resistance. In contrast, the cell with HMA-41 only display one semicircle (Figure S20). The battery based on the HMA-41 also possessed extremely long cycle life with a low-capacity decay of 0.013% per cycle over 3,500 cycles at 3 C (Figure 4E). Comparing to reported MXene-based and other multifunctional ones including carbon-based, functional groups-based, and inorganic substance-based separators of Li-S batteries, the HMA-41 separator exhibited a remarkable advantage in improving the cycle life and capacity retention over long term at various current rates (Figure 4D and Tables S4 and S5). In order to obtain the high energy density of Li-S batteries for practical application, the cells with high sulfur loading of 3.0, 4.5, and 6.0 mg cm^{-2} with a control E/S ratio of 8:1 were also prepared (see experimental procedures). Notably, a high reversible specific/areal capacity of 6.1 mAh cm^{-2} at 0.1 C was achieved at a sulfur loading of 6.0 mg cm^{-2} (Figure 4F). Similar to the case of low sulfur loading, the capacity of the cell recovered to 5.4 mAh cm^{-2} when the current rate was switched back to 0.2 C due to the fast ion transfer and the strong ability to suppress LPS crossover (Figure 4G). In the following 200 cycles, the cell still exhibited excellent cycling stability, which is highly competitive with most cells with sulfur content $\geq$3.0 mg cm^{-2} (Figure 4H and Table S6).

Dendrite suppression

The uncontrolled lithium dendrite growth upon charging is another major issue of Li-S batteries. HMA-41 membranes were also assembled into symmetric Li/separator/Li coin cells to further exemplify the suppression of lithium dendrites (Figure 5). At a current density of 3 mA cm^{-2}, the control cell with Celgard 2400 showed a steady increase in its voltage profile from the 1-h cycling at 0.1 V to the 300-h cycling at 0.02 V (Figure 5A). As for the cell with HMA-41, a flat voltage profile was maintained at 0.1 V from the 1-h cycling to the 450-h cycling (Figure 5A). The steady voltage profile for cells with HMA-41 suggests that lithium dendrites were effectively suppressed. To investigate the evolution of the voltage profiles in detail, the cycling

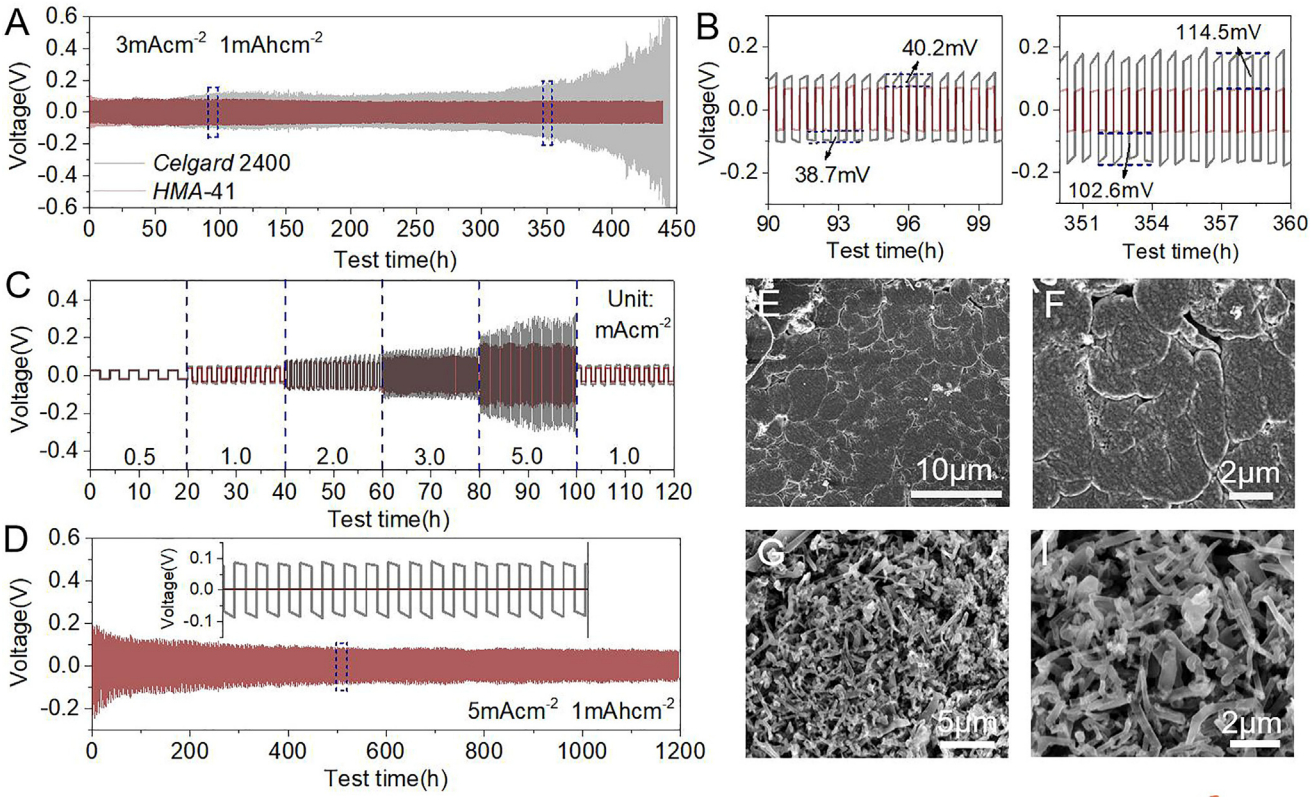

Figure 5. Cycling stability of the Li-S batteries with HMA-41 separator

(A and B) Comparison of the cycling stability of the HMA-41 and the Celgard 2400 separator at a current density of 3 mA cm^{-2} with a stripping/plating capacity of 1 mAh cm^{-2}.

(C) The cycling stability of the HMA-41 and the Celgard 2400 separator with various current densities from 0.5 to 5.0 mA cm^{-2} with a stripping/plating capacity of 1 mAh cm^{-2}.

(D) Long-term cycling of HMA-41 separator over 1,200 h.

(E–H) SEM images of the lithium electrode with HMA-41 and Celgard 2400 separator after 450-h cycles at a current density of 3 mA cm^{-2} with a stripping/plating capacity of 1 mAh cm^{-2}.

of the cells with HMA-41 and Celgard 2400 separator was further enlarged (Figure 5B). The constant cycling voltage profiles at both the charging and discharging states can be well maintained without apparent amplification in hysteresis for cells throughout the whole cycle with HMA-41, whereas batteries with Celgard 2400 exhibited pronounced oscillating voltage profiles with higher overpotential at the stage of stripping/plating promoting the growth of dendrites. When the current density further increases to 5 mA cm^{-2}, this phenomenon becomes more pronounced, and Celgard 2400 exhibits a gradual increase of the hysteresis, which is caused by the unstable electrode/electrolyte interface due to the repeated growth of dendrites. (Figure 5C). In contrast, the cell with HMA-41 still operates stably for a more extended period (Figure 5D). Celgard 2400 and HMA-41 separators were pressed into the soft lithium electrode. A cell was subjected to multiple fast, incomplete charge-discharge cycles following the capacitance fade and the battery voltage similar to the experimental series in Figure 5C. The shortening of the battery resulted in a drastic reduction of both. The nanoscale morphology of nacre-like HMA-41 membranes directly correlates with the ability to suppress dendrites (Figures 5E and 5F). We examined that the average distance between the ANF mesh in the outermost layer of the HMA-41 membrane determines dendrite

suppression. Despite the formation of dendrites promoted through high charging/discharging cycles, the Li electrode surface from HMA-41 remained consistently flat (Figures 5E and 5F) in comparison to the rough and heavily dendritic electrode surface from Celgard 2400 (Figures 5G and 5H), further demonstrating the advantages of HMA-41 membranes.

In conclusion, a multifunctional biomimetic HMA-41 separator integrating a hierarchical ion "highway" and nacre-like architecture has been introduced for Li-S cells to mitigate the loss of active material, eliminate obstacles of ion transport, and suppress dendrite growth on the anode. The physical and chemical barrier provided by the coexistence of negative charges of the HMA-41 separator, efficient Li^+ transport, as well as the lithium dendrite growth suppression leads to the exceptional electrochemical performances observed in the Li-S battery. This nacre-inspired HMA-41 separator provides important clues in the future development of Li-S batteries and may be broadly adapted in other energy-storage technologies.

EXPERIMENTAL PROCEDURES

Resource availability

Lead contact

Further information and requests for resources and reagents should be directed to, and will be fulfilled by, the lead contact Mingqiang Wang (mqwang@hit.edu.cn).

Materials availability

This study did not generate new unique reagents.

Data and code availability

The authors declare that data supporting the findings of this study are available within the article and the supplemental information. All other data are available from the lead contact upon reasonable request.

Materials

Ti_3AlC_2 (98%, 400 mesh) was purchased from Jilin 11 Technology Co. Bulk Kevlar 69 was purchased from Dupont Company. Hydrochloric acid (37 wt %) was provided by Xilong Scientific Co. Lithium fluoride (99.99%, metals basis), KOH, DMSO (99.7%), polyvinylidene fluoride binder, *N*-methylpyrrolidone, lithium bis(trifluoromethanesulfonyl)imide, 1,2-dimethoxyethane, 1, 3-dioxolane, lithium nitrate, lithium sulfide (Li_2S), and sulfur were purchased from Sigma-Aldrich. All chemical reagents were used as received without any further purification.

Synthesis and characterization

Full experimental procedures are provided in the supplemental experimental procedures.

SUPPLEMENTAL INFORMATION

Supplemental information can be found online at https://doi.org/10.1016/j.xcrp.2023.101592.

ACKNOWLEDGMENTS

This work was supported by the Young Elite Scientists Sponsorship Program by CAST (2022QNRC001), China Postdoctoral Science Foundation (grant nos. 2022T150162 and 2020M681091), the Heilongjiang Postdoctoral Fund (grant no. LBH-Z19143), National Natural Science Foundation of China (52303077) and Laboratory of Advanced Materials of Ministry of Education Fund (no. AdvMat-2023-3).

AUTHOR CONTRIBUTIONS

W.Y. and V.C. performed the experiments and analyzed the data. W.S., Z.L., L.L., Z.X., and Y.H. conducted part of the analysis and characterizations. H.Y. and W.M. conceptualized the study, designed the experiments, and contributed to writing the paper. All authors discussed the results and commented on the manuscript.

DECLARATION OF INTERESTS

The authors declare no competing interests.

INCLUSION AND DIVERSITY

We support inclusive, diverse, and equitable conduct of research.

Received: June 19, 2023
Revised: June 24, 2023
Accepted: September 1, 2023
Published: September 22, 2023

REFERENCES

1. Tao, T., Lu, S., Fan, Y., Lei, W., Huang, S., and Chen, Y. (2017). Anode improvement in rechargeable lithium-sulfur batteries. Adv. Mater. *29*, 1700542.

2. Yao, W., Xu, J., Ma, L., Lu, X., Luo, D., Qian, J., Zhan, L., Manke, I., Yang, C., Adelhelm, P., and Chen, R. (2023). Recent progress for concurrent realization of shuttle-inhibition and dendrite-free lithium-sulfur batteries. Adv. Mater. *35*, 202212116.

3. Zhao, Q., Wang, R., Wen, J., Hu, X., Li, Z., Li, M., Pan, F., and Xu, C. (2022). Separator engineering toward practical Li-S batteries: targeted electrocatalytic sulfur conversion, lithium plating regulation, and thermal tolerance. Nano Energy *95*, 106982.

4. Zhang, Q., Huang, Q., Hao, S.M., Deng, S., He, Q., Lin, Z., and Yang, Y. (2022). Polymers in lithium-sulfur batteries. Adv. Sci. *9*, 2103798.

5. Chen, Y., Wang, T., Tian, H., Su, D., Zhang, Q., and Wang, G. (2021). Advances in lithium-sulfur batteries: from academic research to commercial viability. Adv. Mater. *33*, 2003666.

6. Li, Y., and Guo, S. (2021). Material design and structure optimization for rechargeable lithium-sulfur batteries. Matter *4*, 1142–1188.

7. Fu, A., Wang, C., Pei, F., Cui, J., Fang, X., and Zheng, N. (2019). Recent advances in hollow porous carbon materials for lithium-sulfur batteries. Small *15*, 1804786.

8. Hu, G., Xu, C., Sun, Z., Wang, S., Cheng, H.M., Li, F., and Ren, W. (2016). 3D graphene-foam-reduced-graphene-oxide hybrid nested hierarchical networks for high-performance Li-S batteries. Adv. Mater. *28*, 1603–1609.

9. Wang, Z., Tang, Y., Fu, X., Wang, J., Peng, Z., Zhang, L., and Huang, J. (2020). In situ imaging polysulfides electrochemistry of Li-S batteries in a hollow carbon nanotubule wet electrochemical cell. ACS Appl. Mater. Interfaces *12*, 55971–55981.

10. Cao, Y., Liu, C., Wang, M., Yang, H., Liu, S., Wang, H., Yang, Z., Pan, F., Jiang, Z., and Sun, J. (2020). Lithiation of covalent organic framework nanosheets facilitating lithium-ion transport in lithium-sulfur batteries. Energy Storage Mater. *29*, 207–215.

11. Cheng, H., Zhang, S., Li, S., Gao, C., Zhao, S., Lu, Y., and Wang, M. (2022). Engineering Fe and V coordinated bimetallic oxide nanocatalyst enables enhanced polysulfides mediation for high energy density Li-S battery. Small *18*, 2202557.

12. Zhou, L., Danilov, D.L., Eichel, R., and Notten, P.H.L. (2020). Host materials anchoring polysulfides in Li-S batteries reviewed. Adv. Energy Mater. *11*, 2001304.

13. Gao, G., Sun, X., and Wang, L.W. (2020). An inverse vulcanized conductive polymer for Li-S battery cathodes. J. Mater. Chem. A *8*, 21711–21720.

14. Ni, X., Qian, T., Liu, X., Xu, N., Liu, J., and Yan, C. (2018). High lithium ion conductivity HIF/GO solid electrolyte interphase inhibiting the shuttle of lithium polysulfides in long-life Li-S batteries. Adv. Funct. Mater. *28*, 1706513.

15. Liu, B., Taheri, M., Torres, J.F., Fusco, Z., Lu, T., Liu, Y., Tsuzuki, T., Yu, G., and Tricoli, A. (2020). Janus conductive/insulating microporous ion-sieving membranes for stable Li-S batteries. ACS Nano *14*, 13852–13864.

16. Ren, W., Zheng, Y., Cui, Z., Tao, Y., Li, B., and Wang, W. (2021). Recent progress of functional separators in dendrite inhibition for lithium metal batteries. Energy Storage Mater. *35*, 157–168.

17. Wang, M., Vecchio, D., Wang, C., Emre, A., Xiao, X., Jiang, Z., Bogdan, P., Huang, Y., and Kotov, N.A. (2020). Biomorphic structural batteries for robotics. Sci. Robot. *5*, eaba1912.

18. Liu, X., Huang, J.Q., Zhang, Q., and Mai, L. (2017). Nanostructured metal oxides and sulfides for lithium-sulfur batteries. Adv. Mater. *29*, 1601759.

19. Yue, J., Yan, M., Yin, Y.X., and Guo, Y.G. (2018). Progress of the interface design in all-solid-state Li-S batteries. Adv. Funct. Mater. *28*, 1707533.

20. Ghazi, Z.A., He, X., Khattak, A.M., Khan, N.A., Liang, B., Iqbal, A., Wang, J., Sin, H., Li, L., and Tang, Z. (2017). MoS_2/Celgard separator as efficient polysulfide barrier for long-life lithium-sulfur batteries. Adv. Mater. *29*, 1606817.

21. Xu, J., An, S., Song, X., Cao, Y., Wang, N., Qiu, X., Zhang, Y., Chen, J., Duan, X., Huang, J., et al. (2021). Towards high performance Li-S batteries via sulfonate-rich COF-modified separator. Adv. Mater. *33*, 2105178.

22. Wang, M., Emre, A.E., Kim, J.Y., Huang, Y., Liu, L., Cecen, V., Huang, Y., and Kotov, N.A. (2022). Multifactorial engineering of biomimetic membranes for batteries with multiple high-performance parameters. Nat. Commun. *13*, 278.

23. Zhao, H., Yue, Y., Zhang, Y., Li, L., and Guo, L. (2016). Ternary artificial nacre reinforced by ultrathin amorphous alumina with exceptional mechanical properties. Adv. Mater. *28*, 2037–2042.

24. Zeng, G., Liu, Y., Chen, D., Zhen, C., Han, Y., and He, W. (2021). Natural lepidolite enables fast polysulfide redox for high-rate lithium sulfur batteries. Adv. Energy Mater. *11*, 2102058.

25. Z, Y., F.,H., and F.,B.. (2019). Impact resistant nacre-like transparent materials. Mater. Sci. *364*, 1260–1264.

26. Mao, L.B., Gao, H.L., Yao, H.B., Liu, L., Cölfen, H., Liu, G., Chen, S.M., Li, S.K., Yan, Y.X., Liu, Y.Y., and Yu, S.H. (2016). Synthetic nacre by predesigned matrix-directed mineralization. Science *354*, 107–110.

27. Zheng, C., Yao, Y., Rui, X., Feng, Y., Yang, D., Pan, H., and Yu, Y. (2022). Functional Mxene-based materials for next-generation rechargeable batteries. Adv. Mater. *34*, 2204988.

28. Wei, C., Xi, B., Wang, P., Liang, Y., Wang, Z., Tian, K., Feng, J., and Xiong, S. (2023). In situ

anchoring ultrafine ZnS nanodots on 2D Mxene nanosheets for accelerating polysulfide redox and regulating Li plating. Adv. Mater. *35*, 55971–55981.

29. Yang, B., Guo, D., Lin, P., Zhou, L., Li, J., Fang, G., Wang, J., Jin, H., Chen, X., and Wang, S. (2022). Hydroxylated multi-walled darbon nanotubes covalently modified with tris(hydroxypropyl) phosphine as a functional interlayer for advanced lithium-sulfur batteries. Angew. Chem., Int. Ed. Engl. *61*, e202204327.

30. Wang, P., Sun, F., Xiong, S., Zhang, Z., Duan, B., Zhang, C., Feng, J., and Xi, B. (2022). WSe_2 flakelets on N-doped graphene for accelerating polysulfide redox and regulating Li plating. Angew. Chem. Int. Ed. *61*.

31. Chen, C., Yang, G., Liu, D., Wang, X., Kotov, N.A., and Lei, W. (2022). Aramid nanofiber membranes for energy harvesting from proton gradients. Adv. Funct. Mater. *32*, 2102080.

32. Li, P., Lv, H., Li, Z., Meng, X., Lin, Z., Wang, R., and Li, X. (2021). The electrostatic attraction and catalytic effect enabled by ionic-covalent organic nanosheets on Mxene for separator modification of lithium-sulfur batteries. Adv. Mater. *33*, 2007803.

33. Wang, Y., Richards, W.D., Ong, S.P., Miara, L.J., Kim, J.C., Mo, Y., and Ceder, G. (2015). Design principles for solid-state lithium superionic conductors. Nat. Mater. *14*, 1026–1031.

34. Yin, Y.X., Xin, S., Guo, Y.G., and Wan, L.J. (2013). Lithium-sulfur batteries: electrochemistry, materials, and prospects. Angew. Chem., Int. Ed. Engl. *52*, 13186–13200.

35. Ji, H., Wang, Z., Sun, Y., Zhou, Y., Li, S., Zhou, J., Qian, T., and Yan, C. (2023). Weakening Li+ De-solvation barrier for cryogenic Li–S pouch cells. Adv. Mater. *35*, 2208590.

36. Tian, W., Vahid Mohammadi, A., Reid, M.S., Wang, Z., Ouyang, L., Erlandsson, J., Pettersson, T., Wågberg, L., Beidaghi, M., and Hamedi, M.M. (2019). Multifunctional nanocomposites with high strength and capacitance using 2D Mxene and 1D nanocellulose. Adv. Mater. *31*, 1902977.

37. Yang, B., Wang, L., Zhang, M., Li, W., Zhou, Q., and Zhong, L. (2021). Advanced separators based on aramid nanofiber (ANF) membranes for lithium-ion batteries: a review of recent progress. J. Mater. Chem. A *9*, 12923–12946.

38. Guan, Y., Li, W., Zhang, Y., Shi, Z., Tan, J., Wang, F., and Wang, Y. (2017). Aramid nanofibers and poly (vinyl alcohol) nanocomposites for ideal combination of strength and toughness via hydrogen bonding interactions. Compos. Sci. Technol. *144*, 193–201.

39. Li, Y., Li, M., Zhu, Y.C., Song, S., Li, S.N., Aarons, J., Tang, L.C., and Bae, J. (2023). Polysulfide-inhibiting, thermotolerant and nonflammable separators enabled by DNA Co-assembled CNT/Mxene networks for stable high-safety Li-S batteries. Composites, Part B *251*, 110465.

40. Xiong, D., Huang, S., Fang, D., Yan, D., Li, G., Yan, Y., Chen, S., Liu, Y., Li, X., Von Lim, Y., et al. (2021). Porosity engineering of Mxene membrane towards polysulfide inhibition and fast lithium ion transportation for lithium-sulfur batteries. Small *17*, 2007442.

41. Gu, S., Jiang, H., Li, X., Dai, Y., Zheng, W., Jiang, X., and He, G. (2022). Dispersing single-layered $Ti_3C_2T_x$ nanosheets in hierarchically-porous membrane for high-efficiency Li^+ transporting and polysulfide anchoring in Li-S batteries. Energy Storage Mater. *53*, 32–41.

42. Shaibani, M., Akbari, A., Sheath, P., Easton, C.D., Banerjee, P.C., Konstas, K., Fakhfouri, A., Barghamadi, M., Musameh, M.M., Best, A.S., et al. (2016). Suppressed polysulfide crossover in Li-S batteries through a high-flux graphene oxide membrane supported on a sulfur cathode. ACS Nano *10*, 7768–7779.

43. Zhou, G., Chen, H., and Cui, Y. (2022). Formulating energy density for designing practical lithium-sulfur batteries. Nat. Energy *7*, 312–319.

44. Jin, Q., Qi, X., Yang, F., Jiang, R., Xie, Y., Qie, L., and Huang, Y. (2021). The failure mechanism of lithium-sulfur batteries under lean-ether-electrolyte conditions. Energy Storage Mater. *38*, 255–261.

45. Qi, X., Yang, F., Sang, P., Zhu, Z., Jin, X., Pan, Y., Ji, J., Jiang, R., Du, H., Ji, Y., et al. (2023). Electrochemical reactivation of dead Li_2S for Li-S batteries in non-solvating electrolytes. Angew. Chem., Int. Ed. Engl. *135*, 202218803.